Characterizing the depth of cover across South Australia: A simple passive-seismic method for estimating sedimentary thickness

Shubham Agrawal[1]*, Caroline M. Eakin[1], and John O'Donnell[2]

[1] Research School of Earth Sciences, Australian National University, Canberra, Australia.

[2] Geological Survey of South Australia, Department for Energy and Mining, Adelaide, Australia.

Email: shubham.agrawal@anu.edu.au (Shubham Agrawal); caroline.eakin@anu.edu.au (Caroline Eakin); John.O'Donnell2@sa.gov.au (John O'Donnell)

This manuscript is a preprint and has been submitted for publication in Bulletin of the Seismological Society of America. Please note that, the manuscript status is under peer-review, the manuscript has yet to be formally accepted for publication.

*Corresponding author: Shubham Agrawal (shubham.agrawal@anu.edu.au)

Abstract

A blanket of sedimentary and regolith material covers approximately three-quarters of the Australian continent. This poses a significant exploration challenge, with future mineral and energy resources discoveries likely confined beneath the sedimentary cover. The most fundamental question that can be asked is how thick are the sediments? Borehole drilling and active seismic experiments provide excellent constraints, but they are limited in geographical coverage due to their expense, especially when operating in remote areas. On the other hand, passive-seismic deployments are relatively low-cost and portable, providing a practical alternative for initial surveys. Here we introduce a technique utilizing receiver functions for both temporary and permanent seismic stations in South Australia. We present a straightforward method to determine the basement depth based on the arrival time of the P-converted-to-S phase generated at the boundary between crustal basement and sediments. Our results provide an excellent match with the available borehole data, allowing for a simple predictive relationship between Ps arrival time and basement depth to be established. Our method thus opens a way to determine the basement depth in unexplored areas requiring only temporary seismic stations deployed for < 6 months.

Key words:

1. Characterizing the depth of sedimentary cover is critically important for future exploration; however current methods can be prohibitively expensive.
2. We devise a receiver function based method to quickly and cheaply determine the basement depth employing temporary seismic stations.
3. We demonstrate the applicability of our method to South Australia for sedimentary basin thickness ranging up to 2600 m.

Introduction

The Australian continent is the flattest and one of the most tectonically stable continents on Earth, with the last major mountain-building event occurring ~250 Ma (Pain et al., 2012). As a result, around ~80% of the surface of Australia is masked by sediments, predominately Phanerozoic in age, obscuring the underlying crustal basement. Onshore sedimentary basins vary in thickness, ranging from a few hundred meters to up to 15,000 m thick in the Fitzroy Trough within the Canning Basin, northwest Australia (Yeates et al., 1984). Many of these basins host rich natural resources, such as base metals (and their subsidiaries), hydrocarbons, and groundwater (e.g. Hitzman et al., 2010; Leach et al., 2010). For instance, significant oil and gas reserves can be found in the Cooper and Eromanga Basins of central Australia. Recent studies focusing on Australia have suggested that 15% of Australia is a prospective target for sediment-hosted deposits (Hoggard et al., 2020). The abundance of Archean and Proterozoic blocks in Australia provides a potentially fruitful avenue for future explorations as sediment-hosted metal minerals systems are largely associated with Proterozoic basins (e.g. Hitzman et al., 2010; Leach et al., 2010). A known example would be the Carpentaria Zinc Belt within the North Australian Basin System which contains three of the ten largest zinc-lead deposits globally (e.g. Southgate et al., 2013).

Australia's economy is heavily supported by natural resources and mining activity; however the majority of the easily accessible near-surface resources have already been found and, to a large degree, exploited (Mudd et al., 2019; Mudd, 2007). As such, the UNCOVER Initiative has become a national priority (Collett and McFadden, 2014), with the aim to improve the discovery potential of new mineral deposits currently hidden beneath cover and thus keep pace with increasing global demand (Ali et al., 2017). Constraining the sediment thickness (i.e., depth of cover) is a fundamental component within this UNCOVER Initiative, under the core theme of "characterizing Australia's cover".

The most accurate estimates of sediment thickness come from borehole drilling followed by active-source seismic surveys. While both provide excellent constraints, they are expensive (especially for deep boreholes) and require heavy machinery, which can be logistically difficult to dispatch to remote locations. As an alternative, passive-source seismology is non-invasive, relatively low-cost, and with portable instrumentation (i.e. seismometers) that is easier to transport and deploy to remote locations (Rawlinson et al., 2017). Several passive-source seismic techniques currently exist to study the near-surface structure, such as the horizontal to vertical spectral ratio (commonly referred to as HVSR), spatial autocorrelation coefficient method, and using the ambient seismic wavefield (e.g. Lunedei and Albarello, 2010; Okada, 2006). Here we demonstrate the feasibility of using passive recording by single-station seismometers to infer the depth to crystalline basement directly. We use the arrival information of the P-to-S converted phase from the top of crustal basement. Utilizing a recent expanse in passive seismic deployments across South Australia (supplement Figure **S1**), and a wealth of existing drilling data in regions of exploration, we show a remarkable relationship between P-to-S arrival time and the depth of basement. This relationship is calibrated from the existing data and applied to predict the sediment thickness in under-explored remote regions where recent seismic deployments have occurred. The method we employ is simple and straightforward to use, typically requiring only a few months of recorded data and is dependent only on the thickness of the sediments and their Poisson's ratio.

[Figure 1 about here.]

Sediment distribution and history of South Australia

South Australia has a rich geological history that stretches as far back as the Archean, with the origin of the Gawler Craton, the largest crustal province in South Australia (Hand et al., 2007). Within the craton lies Olympic Dam, the world's largest uranium resource, with significant copper and gold reserves as well (e.g. Reid, 2019). Much of the mineral rich Gawler Craton, and indeed South Australia in general, is obscured by sediments, with around a dozen or more major sedimentary basins across the state (Figures 1 & 2). Sediment thickness within these basins varies from 0 to > 3,500 m, owing to a lengthy history of spatially varying sedimentation (Wopfner et al., 1969).

The oldest basin within South Australia is the Mesoproterozoic Cariewerloo Basin, with a minimum depositional age of 1,424±51 Ma (Fanning et al., 1983). This intracratonic basin holds dominantly fluvial sandstones with thicknesses up to 1,500 m and holds potential for uranium mineralization (Beyer et al., 2018). The second oldest is the Officer Basin, a large intra-cratonic basin of Neoproterozoic-Devonian age that extends west into Western Australia. Within South Australia, the basement depth exceeds 3,000 m (Wopfner et al., 1969). The Officer Basin is poorly explored, with limited boreholes and no commercial discoveries. The Warburton Basin is the oldest Paleozoic basin in South Australia (Cambrian-Ordovician age) and overlies the Proterozoic basement in the north-east part of the state (Gatehouse, 1986). The basin is demarcated into west and east by uplifted basement under the Birdsville Track Ridge, with the east Warburton studied more extensively as it underlies the oil and gas producing Cooper and Eromanga Basins (Radke, 2009). The Early to Middle Cambrian Arrowie Basin comprises three separated areas from Flinders Ranges to the border with New South Wales (Zang et al., 2004). The thickest sediments are in the central part with values greater than 3,000 m. The early Paleozoic Pedrika and Arckaringa Basins are largely under-explored, with Permian sediment thickness reaching 1,000 m in certain areas (Drexel and Preiss, 1995). The Cooper Basin, comprising Middle Triassic to Permian non-marine sequences, is perhaps the best-studied basin in South Australia owing to prolific oil and gas reserves. The basin's long axis trends northeast-southwest and the predominantly gas reserves are located 1,250 m below the surface (Radke, 2009). In contrast, the overlying Jurassic-Cretaceous Eromanga Basin hosts mostly oilfields (Radke, 2009). The Eromanga Basin is more extensive, fully covering the Cooper and Warburton Basins, extending to the western boundaries of Pedirka and Arckaringa Basins, and further north and east into central Queensland and New South Wales (Wopfner et al., 1969). The Mesozoic Bight and Otway Basins have significant offshore sediments and potential for explorations (Drexel and Preiss, 1995). Otway, in particular, has notable onshore sediments with thickness of more than 3,000 m, as detected by borehole measurements (Figure 2). The Mesozoic Berri Basin is completely concealed beneath the Murray Basin with basement depths up to 600 m (Brown and Stephenson, 1991). Most recently, during the Cenozoic, three large-scale sedimentation episodes occurred, namely Eucla (extends 500 km offshore), Murray, and Lake Eyre Basin (Brown and Stephenson, 1991; Drexel and Preiss, 1995).

Given the abundance of sedimentary basins and associated sub-surface natural resources in South Australia, there have been more than 27,100 onshore boreholes drilled (see Data and Resources Section) that determined the depth to basement (Figure 2). The basement depth values range between 0-3698 m, with the deepest values in the Cooper-Eromanga Basin area around Moomba. The vast majority ($\sim$94%) of boreholes have been drilled in places with sediment thickness less than 200 m (supplement Figure **S2**). The highest concentration of deeper boreholes (> 1400 m) is within the Cooper-Eromanga Basin, with more than 900 boreholes drilled to the basement.

[Figure 2 about here.]

Data and Methods

Receiver functions in sediments

Receiver functions (RFs) are an effective and commonly used tool to image seismic discontinuities within the Earth's crust and mantle arising from changes in the material properties. The RF technique focuses on converted phases - typically P to S conversions (Ps) in the P-wave coda - arising from seismic velocity discontinuities below the receiver (i.e. a seismic station)(Ammon, 1991; Langston, 1979; Vinnik, 1977). To remove the effect of source-side structure and wavefield propagation, the vertical component (dominated by P-wave energy) is deconvolved from the radial component seismogram (containing energy from both P and S waves) to obtain the radial RF, hereafter simply referred to as the RF (e.g. Ligorría and Ammon, 1999).

RFs have been employed extensively to image the Moho (crust-mantle boundary), the lithosphere-asthenosphere boundary, and the 410 km and the 660 km global seismic discontinuities. (e.g. Birkey et al., 2021; Kennett et al., 2011; Tauzin et al., 2013). However, only a few have used RFs to constrain the properties of the sedimentary layers without forward modeling (e.g. Cunningham and Lekic, 2020; Piana Agostinetti et al., 2018; Srinivas et al., 2013; Yeck et al., 2013; Yu et al., 2015; Zheng et al., 2005). In the presence of a sedimentary layer, RFs are dominated by strong reverberations after the arrival of the direct-P phase. These can last for several seconds and can mask the signal from deeper crustal discontinuities (e.g. Tao et al., 2014; Zelt and Ellis, 1999). This occurs due to the significant impedance contrast between the low-velocity sedimentary layer and the basement rock, trapping the P and S waves in the sediment layer. The presence of a sedimentary layer has some additional customary effects on the RF signal. When the incoming teleseismic P-wave enters the low-velocity sediments, the angle of incidence steepens (due to Snell's Law), and the ray becomes nearly vertical (Figure 3). The energy of the direct-P wave is, therefore mostly confined to the vertical component, with minimal energy on the horizontal components (radial and transverse). The amplitude of the first P-arrival on the radial RF, therefore, decreases as the incidence angle steepens and the pulse width is broadened (Sheehan et al., 1995; Zelt and Ellis, 1999). Instead, the P-to-S converted phase between the basement and sediments often becomes the strongest amplitude signal on the radial RF, and can completely mask the low amplitude direct P-wave (Cunningham and Lekic, 2020; Yeck et al., 2013; Yu et al., 2015). We term this phase Ps_b and focus on its arrival time on the radial RF relative to the direct P-arrival on the vertical RF to estimate the depth to basement. Both an increase in Poisson's ratio (larger V_p/V_s ratio) and the thickness of the sedimentary layer leads to a later arrival of the Ps_b phase (Zelt and Ellis, 1999).

Seismic stations and receiver function computation

In the last several years, there has been an expansion in the number of passive seismic deployments across South Australia (supplement Figure **S1**). While coverage is still non-uniform and occasionally sparse, the addition of new networks in increasingly remote locations allows for the investigation of Earth's structure in under-explored regions within the continental interior that are typically less accessible to other methods. Most recently, the Marla Line (Liang and Kennett, 2020), Lake Eyre Basin (Eakin, 2019), and AusArray-SA (O'Donnell et al., 2020) experiments have increased coverage over the eastern margin of the Gawler Craton, and the various sedimentary sequences that cover it. The Lake Eyre Basin seismic array, as the name suggests, has increased coverage surrounding Kati Thanda-Lake Eyre and was also the first to install passive-recording seismometers in the Simpson Desert, where the sediment thicknesses are greatest within South Australia. This vast sandy desert contains the world's longest parallel sand dunes and was not crossed by motorized vehicle until 1962 (Wakelin-King and White, 2016).

Overall data from twelve temporary and two permanent seismic networks (AU and S1), with stations located across South Australia, were used for analysis in this study (see Data and Resources Section; supplement Figure **S1**). In addition, some stations situated just beyond the state borders were included where available, such as the AQT network (1Q) in southwest Queensland. For the Marla Line experiment (3G), which had dense station spacing of < 4km, we selected only every 5th station. Both short-period and broadband seismic stations (channels SH*, HH*, BH*, and EH*) were utilized for the receiver function analysis, comprising 243 individual seismic stations in total.

For each station, three-component data for earthquakes of Mw $\geq$ 5.5 and in the distance range of 30° – 95° was sought (Figure **S3** shows an example of earthquakes available for the station AEB15). For temporary networks, typically, a minimum of four months recording provided more than 75 earthquakes; however, on average, more than 150 earthquakes were available for each station. For permanent stations, earthquakes were sought from the previous year (2020), as this provided sufficient RFs for the analysis. The extracted 200 s of seismograms around the expected (using iasp91; Kennett and Engdahl, 1991) teleseismic P-arrival (50 s before and 150 s after) were then demeaned, detrended (linear), cosine tapered, and bandpass filtered between 0.1-1 Hz. Only earthquakes with a signal-to-noise ratio $\geq$ 1.5 (noise window: 45 s to 15 s prior to predicted P; signal window: 5 s before to 25 s after predicted P) were kept. The radial RFs were computed through the 'rf' Python-package (Eulenfeld, 2020), using an iterative time-domain deconvolution (Ligorría and Ammon, 1999). Each RF was then stretched and compressed on the time axis using a reference slowness of 6.4 s/° (moveout correction) since the arrival times of converted phases are influenced by the slowness of the ray as well. Further, to ascertain the quality of individual RFs and the subsequent stacks, only radial RFs where the largest arrival is a positive polarity peak within the first 2 s were kept. Stations with at least ten good RFs were then stacked (an example is shown in Figure 3c). Out of 243 stations, 231 met this criterion and were used for further analysis. All 231 stacked RFs are presented in supplement Figure **S4** and the corresponding list of measurements in supplement Table **S1**.

[Figure 3 about here.]

Using the RF stack for each station, the $\mathrm{Ps_b}$ arrival time (i.e. the P-wave converted to S-wave at the basement-sediment boundary) was determined with respect to the direct P-wave arrival on the vertical receiver function hereafter referred to as $T_{\mathrm{Ps_b}}$. As illustrated in Figure 3, in the presence of sediments, the direct P-wave has near-vertical incidence beneath the seismic station and thus has a small amplitude on the radial RF. Instead, the largest positive peak on the radial RF is the $\mathrm{Ps_b}$ phase, which arrives shortly after ($\sim$1 s for station AEB07) the direct P on the vertical RF. The relative time difference between the largest positive peak on the radial RF and the vertical RF is, therefore, simply measured for each station to estimate $T_{\mathrm{Ps_b}}$, which is primarily a function of the sediment thickness (Figure 3).

Results and Discussion

Spatial variation of $T_{\mathrm{Ps_b}}$

The obtained $T_{\mathrm{Ps_b}}$ values for all 231 stations reveal striking geographical patterns (Figure 4). The $T_{\mathrm{Ps_b}}$ values are highest in the northeast of the study area while lowest for stations on the southern Gawler Craton. The highest $T_{\mathrm{Ps_b}}$ value of 1.32 s was recorded at station SB03 (Skippy network; 7B) situated atop the Cooper and Eromanga Basins. The majority (61%) of stations registered $T_{\mathrm{Ps_b}}$ $\leq$ 0.2 s, while 16 stations ($\sim$ 7%) had $T_{\mathrm{Ps_b}} \geq 1$ s.

Areas of elevation and outcropping basement - such as the southern Gawler Craton, Flinders Ranges, and Musgrave Province - have $T_{\mathrm{Ps_b}}$ values close to zero, indicating minimal sedimentation in such regions (gray areas in Figure 4). On a smaller scale, stations OOD, AEB17, SD06, and AES15 installed on top of the Denison and Peake Inliers (DPI in Figure 2), a small basement outcrop to the west of Kati Thanda-Lake Eyre, display $T_{\mathrm{Ps_b}} \sim 0$ s, while surrounded by stations with $T_{\mathrm{Ps_b}} \geq 0.4$ s that lie beyond the basement inlier. Moderate values of $T_{\mathrm{Ps_b}}$ ($\sim$0.5 s) are co-located with regions with significant sediment accumulation, such as the Berri, Arrowie, Bight, and Arckaringa Basins. The highest values of $T_{\mathrm{Ps_b}}$ ($\sim$1 s or more) are located in regions with several overlapping sedimentary sequences, such as in the northeast where the Lake Eyre, Eromanga, Cooper, and Warburton Basins overlap. Surprisingly, for stations situated on top of the oldest basins such as Officer and Cariewerloo Basins, the $T_{\mathrm{Ps_b}}$ values are close to zero ($\leq$ 0.2 s). Nonetheless, it is evident from the above that the $T_{\mathrm{Ps_b}}$ variations capture both small-scale and large-scale sedimentary features, and therefore can be utilized to estimate the depth to basement beneath each seismic station.

[Figure 4 about here.]

Calibration of $T_{\mathrm{Ps_b}}$ with borehole basement depth

Due to the resource potential, South Australia has an expansive dataset of borehole drill sites (Figure 2). This offers a unique opportunity to compare and calibrate the relationship between $T_{\mathrm{Ps_b}}$ and the basement depth. Of the 243 seismic stations located in South Australia (Figure 4), 85% are located within 0.5° of a borehole site. It is often the case, however, that the seismic stations are located near multiple boreholes; therefore, in order to directly compare, an average value of borehole basement depth must be calculated for each station. We chose to interpolate the borehole basement depth values surrounding each station using the inverse distance weighting (IDW) method (Shepard, 1968). This method assigns a single basement depth value based on a weighted average of the borehole values within 0.5° of a station. If no borehole measurement was found within 0.5° of a station, no basement depth was assigned to it. The weighting given to each borehole value is based on the inverse of the distance to the station to the power of p, chosen here as 2. This takes into account the relative proximity of borehole points to the stations, thus making sure the interpolated basement depth at a station is dominated by the values which are closest and is less likely to be skewed by a single aberrant value.

[Figure 5 about here.]

The IDW method returned an interpolated basement depth beneath 182 seismic stations, represented as circles in Figure 5. We divide the stations in two categories based on the age of sediments beneath the stations. Stations situated atop Phanerozoic sediments are shown as turquoise circles while stations on predominantly Proterozoic sediments are pink. Although there is some scatter, an overall positive correlation between $T_{\mathrm{Ps_b}}$ and interpolated borehole basement depth can be recognized, with larger $T_{\mathrm{Ps_b}}$ arrival times corresponding to deeper borehole basement depths (Figure 5). This positive trend is reinforced when the median values (with standard deviation) are plotted for each data bin (blue squares with errorbars, Figure 5). The gradient of the trend however is not constant, with basement depths gradually increasing for arrival times between 0 and $\sim$0.6 seconds and more steeply increasing thereafter. A linear regression on the binned median values (blue squares), using standard deviations as the weights, is performed to fit two lines that share $T_{\mathrm{Ps_b}}$ = 0.58 s as a common point (yellow square). If a different common point is chosen, then the residual error increases (supplement Figure **S5**). The fitted straight lines are of the form,

$$D = 366\,T_{\mathrm{Ps_b}}, \qquad \text{for } T_{\mathrm{Ps_b}} < 0.58\,\mathrm{s} \tag{1}$$

and

$$D = 3206.9\,T_{\mathrm{Ps_b}} - 1661.2, \qquad \text{for } T_{\mathrm{Ps_b}} \geqslant 0.58\,\mathrm{s}, \tag{2}$$

where $T_{\mathrm{Ps_b}}$ is in seconds and D is the depth to basement in meters. It is to be noted, however that Equations 1 and 2 represent the best fitting linear trends, but the true relationship between the basement depth and $T_{\mathrm{Ps_b}}$ might not be linear. A best-fitting exponential and quadratic relationship was also explored (supplement Figure **S6**), but both of these yielded higher RMSE values than the linear equations. Further, the non-linear curves diverge rapidly for $T_{\mathrm{Ps_b}}$ > 1.5 s. Additional data from deeper sedimentary basins (basement depth > 4000 m) may help further constrain them in the future.

As noted in Figure 3, basement depth and $T_{\mathrm{Ps_b}}$ are related as,

$$D = \frac{T_{\mathrm{Ps_b}} \times Vp_{\mathrm{sedi}} \times Vs_{\mathrm{sedi}}}{Vp_{\mathrm{sedi}} - Vs_{\mathrm{sedi}}}, \tag{3}$$

where $\mathrm{Vp_{sedi}}$ and $\mathrm{Vs_{sedi}}$ are the average seismic velocities in the sediment layers. It is evident that calibrated Equations 1 and 2 are simplified forms of Equation 3 and that the gradient in Figure 5 is a function of the seismic velocities of the sediments. As expected, deeper sedimentary basins (> 500 m) display a steeper gradient indicating faster seismic velocities that likely result from increased compaction at depth.

While the seismic velocities within sedimentary basins may vary in other settings, for our study region, the calibrated equations (1 and 2) seem to provide a reasonable fit to the available borehole data. We, therefore, use the calibrated equations to estimate the basement depth beneath all seismic stations (Figure 6), hereafter referred to as the RF basement depth.

Comparison of seismically determined basement depth with the pattern of sedimentation across South Australia (SA)

[Figure 6 about here.]

Depth to basement estimated using the RF analysis correlates strongly with the extent of sedimentary basins and spatial trends in sedimentation as suggested by the available borehole data (Figure 6). In the northeastern part of the study region, the RF estimated depths are highest, with values up to 2,600 m, due to the superimposition of Permian-Triassic Cooper and Jurassic-Cretaceous Eromanga Basins. Outside the boundary of Cooper Basin (green colored basin in Figure 6b), the basement depth decreases as seen in the borehole values. AQT network stations in Queensland expand the basement depth knowledge in this region. Station AQTK1, which is inside the Cooper basin, registers a depth of 2,352 m; in comparison, AQT08, located to the northwest outside of the Cooper Basin, records a shallower depth of 620 m, suggesting decreasing sediment thickness moving northwards. South of the Cooper Basin along the SA-NSW border, the basement depth gets progressively shallower (830 m at station CU01 to $\sim$10 m at station E1B1), representing the thinning Eromanga Basin until its southernmost extent near Cockburn (Figure 1). South of Cockburn, the RF basement depth slightly increases again ($\sim$ 150 m) due to the Cenozoic Murray Basin bounded to the west by the Flinders Ranges. Notably, three stations (E1F1, CU35, AURMK) close to the SA-NSW-Victoria border show significantly deeper values ($\sim$ 800 m) due to the presence of the concealed Mesozoic Berri Basin. This adds further constraints to the boundary of Berri Basin, which is more sparsely sampled by borehole drilling (Figure 6a).

Near the border between SA and the Northern Territory (26° S), there is a dramatic change in the RF basement depth around longitude 134° E. East of this location, within the Simpson Desert, the RF estimated depth to the Proterozoic crystalline basement reaches up to 2,500 m due to the combined sediments from the Early Palaeozoic Warburton, Permian–Triassic Pedrika, Eromanga, and Cenozoic Lake Eyre Basins (Gatehouse, 1986; Wopfner et al., 1969). These stations in the Simpson Desert, which belong to the Lake Eyre Basin array, are the first to be deployed in the region, thus providing new basement depth constraints for hitherto under-explored parts of Australia. West of 134° E marks the low-sediment region of the exhumed Musgrave province, the result of the Petermann Orogeny around 570–530 Ma (e.g. Wade et al., 2008). Stations located within the Musgrave province record typically shallow RF basement depths of < 25 m. The Marla Line experiment (3G), a dense east-west linear transect of seismic stations, further illustrates the decreasing sediment thickness from the east (870 m) to the west (10 m) due to thinning of the Eromanga Basin. South of Oodnadatta, four stations (OOD, AEB17, SD06, AES15) show shallower basement depth (< 70 m) compared to the surrounding stations (∼200 m). These stations sit on Neoproterozoic Denison and Peake Inliers surrounded by sediments from Eromanga Basin with Permian Arckaringa Basin sediments to the west (Drexel and Preiss, 1995).

The southern part of the Gawler Craton has areas of exposed Paleoproterozoic-Archean crust with little to no sediment cover, which is well represented by estimated basement depths of < 50 m. However, for stations atop Proterozoic Basins like the Officer, Amadeus, and Cariewerloo Basins the RF basement depths do not match the borehole values (pink circles in Figure 5). Within the boundaries of Mesoproterozoic Cariewerloo Basin, this is especially evident (Fanning et al., 1983), with borehole basement depths of up to 1,500 m. Contrastingly, the RF estimated basement depth is < 100 m. This can be explained as older Proterozoic sediments are often heavily metamorphosed with increased seismic velocities and Vp values potentially greater than 6 km/s (Wang et al., 2016), therefore inhibiting a strong impedance contrast with the crustal basement. Given the propensity of sediment-hosted base metals to be hosted in such Proterozoic basins (Hitzman et al., 2010; Leach et al., 2010), our method may be useful in determining the top of Proterozoic sediments instead. These regions of older and seismically faster Proterozoic basins produce the anomalous cluster of data points in Figure 5 (pink circles) with borehole depth values between 500-1000 m for $T_{\mathrm{Ps_b}} <$ 0.2 s.

Uncertainties in RF basement depth estimation

The RF estimated basement depths appear to match the sedimentary basin and borehole values reasonably well. The typical error expected for any measurement is ±134 m for the shallower (excluding Proterozoic Basins) and ±360 m for the deeper sedimentary basins, as estimated from the size of the error-bars in Figure 5 (i.e. the average standard deviations of the binned data). These typical error ranges are likely influenced by some of the inherent uncertainties underlying our chosen method. One of our primary assumptions is that in the presence of sediments, there is insignificant P-wave energy on the horizontal components; thus, the highest amplitude on the radial RF is due to the $\mathrm{Ps_b}$ phase. However, in regions of thin or well-compacted sediments, this might not always be the case, and there could be a potential overlap of direct P and $\mathrm{Ps_b}$ phase, which may slightly underestimate the RF derived basement depth.

Another assumption is that the largest impedance contrast, representing the first and largest amplitude peak in the RF, is generated by the boundary between the crustal basement and overlying sediments. However, as previously discussed, this appears to be limited by age, and is only applicable for Phanerozoic sediments, not older Proterozoic sedimentary basins. Older sediments are more likely to be metamorphosed, resulting in higher seismic velocities, with less distinction between 'sediments' and the underlying basement. In such cases, the $T_{\mathrm{Ps_b}}$ values can appear anomalously low (< 0.2 s), which may be misinterpreted as a thin layer of sediments (< 200 m) if the geological context is not considered or prior geological information is lacking.

Conclusion and future implications

We present a novel yet simple method to estimate the depth to basement in the presence of varying sediment thickness using receiver functions. Without prior knowledge of the sub-surface velocity structure, the depth to the basement is estimated using the relative arrival time of the P-converted-to-S phase generated at the base of the sediments. The method was demonstrated using data from seismic stations across South Australia and is able to capture the known variations in Phanerozoic sediments across the region. Despite an extensive existing borehole database for South Australia, we are able to improve the basement depth database, particularly in areas of deep sediments and remote areas such as the Simpson, Strzelecki, and Sturt Stony Deserts.

Despite the uncertainties, the methodology showcased here has three main advantages. Firstly, it can be employed to get a quick and credible assessment of sediment thickness using only temporary seismic stations deployed for less than 6 months, with little or no knowledge of the sub-surface velocity structure. Thus, it could serve as a pre-drill strategy to estimate the basement depth before physically deploying drilling equipment. This is particularly beneficial for deep basins, where drilling becomes increasingly expensive for deeper boreholes. Secondly, using temporary seismic stations for a few months is relatively inexpensive, and the acquired passive-seismic data will additionally be useful for many other applications to image the Earth's interior. Thirdly, while our method can't determine the base of Proterozoic basins, it may help determine the top of such metamorphosed sediments, which is desirable for future sediment-hosted base metal exploration projects, especially in places like Australia. Therefore, this method has immense potential for under-explored regions where rich mineral resources may currently be hidden under cover.

Data and Resources

The supplemental figures referenced in the text are included in the accompanying Supplemental Material file. Figure S1 shows the seismic stations available for the study and Figure S4 depicts the individual stacked receiver functions for those stations. An example for earthquakes used for a typical station is shown in Figure S3. Figure S5 and S6 contain four cases of regression analysis where RMSE error was found to be higher than Figure 5. The borehole basement depth variation in South Australia is portrayed in Figure S2 via histograms. Further, Table S1 (uploaded as a separate text file) contains the individual station measurements for $T_{\mathrm{Ps_b}}$ and the estimated basement depth. The earthquakes used in this study were collected from Incorporated Research Institutions for Seismology (IRIS) Data Services (http://ds.iris.edu/ds/, last accessed May 2021). The seismic waveform data from 14 seismic networks was used (last accessed May 2021): 5G (doi:10.7914/SN/5G_2018); 6K (doi:10.7914/SN/6K_2020); 5J (http://www.fdsn.org/networks/detail/5J_2017/); 7B (doi:10.7914/SN/7B_1993); 1F (doi:10.7914/SN/1F_2009); 6F (doi:10.7914/SN/6F_2008); YJ (http://www.fdsn.org/networks/detail/YJ_2009/); 7K (doi:10.7914/SN/7K_2007); 7I (doi:10.7914/SN/7I_2003); 1G (doi:10.7914/SN/1G_2008); 1Q (doi:10.7914/SN/1Q_2016); 3G (doi:10.7914/SN/3G_2018); S1 (doi:10.7914/SN/S1); AU (https://www.fdsn.org/networks/detail/AU/). The Python package 'rf' version 1.0.0 (Eulenfeld, 2020) was used to compute the receiver functions. All the seismic data was handled using the Python package Obspy (https://docs.obspy.org/; Krischer et al., 2015). Borehole data used in the study was obtained from the South Australian Resources Information Gateway and is titled 'Crystalline basement intersecting drillholes'(https://map.sarig.sa.gov.au/; last accessed May 2021). All the geological data used in the study was acquired from the Geoscience Australia Portal (https://portal.ga.gov.au/; last accessed July 2021). Information about the active/operating mines in South Australia was obtained from the Department of Energy and Mining, Government of South Australia (https://energymining.sa.gov.au/; last accessed July 2021).

Plots were made using the Generic Mapping Tools, Version 6.1.1 (https://www.generic-mapping-tools.org/; Wessel et al., 2019) and matplotlib version 3.4.2 (https://matplotlib.org/).

Declaration of Competing Interests

The authors declare no competing interests.

Acknowledgements

The work was supported by Australian Research Council Grant DE190100062. The Lake Eyre Basin seismic array and many other previous temporary deployments were made possible via funding from AuScope (auscope.org.au), instrumentation from the Australian National Seismic Imaging Resource (ANSIR), and contributions from staff at the Research School of Earth Sciences, Australian National University. The AusArray SA deployment is supported by the Geological Survey of South Australia, with instrumentation from ANSIR and Geoscience Australia. The GSSA thanks Bruce Goleby, Ann Goleby, Isaac Axford, Kate Selway, John Stephenson, Alexei Gorbatov, Michelle Salmon, Robert Pickle, and Colin Telfer for their contribution to AusArray SA. We are incredibly grateful to landholders, traditional owners, and the Department of Defence for granting land access for the seismic arrays. JPOD publishes with the permission of the Director of the Geological Survey of South Australia.

References

Ali, S. H., Giurco, D., Arndt, N., Nickless, E., Brown, G., Demetriades, A., Durrheim, R., Enriquez, M. A., Kinnaird, J., Littleboy, A., et al. (2017). Mineral supply for sustainable development requires resource governance. *Nature*, 543(7645):367–372.

Ammon, C. J. (1991). The isolation of receiver effects from teleseismic p waveforms. *Bulletin of the seismological Society of America*, 81(6):2504–2510.

Beyer, S., Kyser, K., Polito, P., and Fraser, G. (2018). Mesoproterozoic rift sedimentation, fluid events and uranium prospectivity in the cariewerloo basin, gawler craton, south australia. *Australian Journal of Earth Sciences*, 65(3):409–426.

Birkey, A., Ford, H. A., Dabney, P., and Goldhagen, G. (2021). The lithospheric architecture of australia from seismic receiver functions. *Journal of Geophysical Research: Solid Earth*, 126(4):e2020JB020999.

Brown, C. M. and Stephenson, A. E. (1991). Geology of the murray basin, southeastern australia. *Bulletin-Australia, Bureau of Mineral Resources, Geology and Geophysics*, (235).

Collett, D. and McFadden, P. (2014). Uncover initiative: ushering in a new era of exploration in australia.

Cunningham, E. and Lekic, V. (2020). Constraining properties of sedimentary strata using receiver functions: An example from the atlantic coastal plain of the southeastern united states. *Bulletin of the Seismological Society of America*, 110(2):519–533.

Drexel, J. and Preiss, W. (1995). The geology of south australia, vol. 2. the phanerozoic: South australia geological survey. *Bulletin*, 55.

Eakin, C. (2019). Seismicity, minerals, and craton margins: The lake eyre basin seismic deployment. *ASEG Extended Abstracts*, 2019(1):1–2.

Eulenfeld, T. (2020). rf: Receiver function calculation in seismology. *Journal of Open Source Software*, 5(48):1808.

Fanning, C., Flint, R., and Preiss, W. (1983). Geochronology of the pandurra formation. *Geological Survey of South Australia Quarterly Geological Notes*, 88:11–16.

Gatehouse, C. G. (1986). The geology of the warburton basin in south australia. *Australian Journal of Earth Sciences*, 33(2):161–180.

Hand, M., Reid, A., and Jagodzinski, L. (2007). Tectonic framework and evolution of the gawler craton, southern australia. *Economic Geology*, 102(8):1377–1395.

Hitzman, M. W., Selley, D., and Bull, S. (2010). Formation of sedimentary rock-hosted stratiform copper deposits through earth history. *Economic Geology*, 105(3):627–639.

Hoggard, M. J., Czarnota, K., Richards, F. D., Huston, D. L., Jaques, A. L., and Ghelichkhan, S. (2020). Global distribution of sediment-hosted metals controlled by craton edge stability. *Nature Geoscience*, 13(7):504–510.

Kennett, B. and Engdahl, E. (1991). Traveltimes for global earthquake location and phase identification. *Geophysical Journal International*, 105(2):429–465.

Kennett, B., Salmon, M., Saygin, E., and Group, A. W. (2011). Ausmoho: the variation of moho depth in australia. *Geophysical Journal International*, 187(2):946–958.

Krischer, L., Megies, T., Barsch, R., Beyreuther, M., Lecocq, T., Caudron, C., and Wassermann, J. (2015). Obspy: A bridge for seismology into the scientific python ecosystem. *Computational Science & Discovery*, 8(1):014003.

Langston, C. A. (1979). Structure under mount rainier, washington, inferred from teleseismic body waves. *Journal of Geophysical Research: Solid Earth*, 84(B9):4749–4762.

Leach, D. L., Bradley, D. C., Huston, D., Pisarevsky, S. A., Taylor, R. D., and Gardoll, S. J. (2010). Sediment-hosted lead-zinc deposits in earth history. *Economic Geology*, 105(3):593–625.

Liang, S. and Kennett, B. L. (2020). Passive seismic imaging of a craton edge–central australia. *Tectonophysics*, 797:228662.

Ligorría, J. P. and Ammon, C. J. (1999). Iterative deconvolution and receiver-function estimation. *Bulletin of the seismological Society of America*, 89(5):1395–1400.

Lunedei, E. and Albarello, D. (2010). Theoretical hvsr curves from full wavefield modelling of ambient vibrations in a weakly dissipative layered earth. *Geophysical Journal International*, 181(2):1093–1108.

Mudd, G., Czarnota, K., Skirrow, R. G., McAlpine, S., Yuan, Y., Yellishetty, M., Weng, Z.-H., and Werner, T. (2019). *Critical Minerals in Australia: A review of opportunities and research needs*. Geoscience Australia.

Mudd, G. M. (2007). *The sustainability of mining in Australia: key production trends and their environmental implications for the future*. Department of Civil Engineering, Monash University.

Okada, H. (2006). Theory of efficient array observations of microtremors with special reference to the spac method. *Exploration Geophysics*, 37(1):73–85.

O'Donnell, J., Thiel, S., Robertson, K., Gorbatov, A., and Eakin, C. (2020). Using seismic tomography to inform mineral exploration in south australia: the ausarray sa broadband seismic array. *MESA Journal*, 93:24–31.

Pain, C. F., Pillans, B. J., Roach, I. C., Worrall, L., and Wilford, J. R. (2012). Old, flat and red–australia's distinctive landscape. *Shaping a nation: A geology of Australia*, pages 227–275.

Piana Agostinetti, N., Martini, F., and Mongan, J. (2018). Sedimentary basin investigation using receiver function: an east african rift case study. *Geophysical Journal International*, 215(3):2105–2113.

Radke, B. (2009). *Hydrocarbon and geothermal prospectivity of sedimentary basins in central Australia: Warburton, Cooper, Pedirka, Galilee, Simpson and Eromanga basins*. Geoscience Australia.

Rawlinson, N., Stephenson, R., and Carbonell, R. (2017). Seismic imaging at the cross-roads: Active, passive, exploration and solid earth. *Tectonophysics*, 718:1–8. Seismix 2016: Advances in active and passive seismic imaging of continents and their margins.

Raymond, O., Totterdell, J., Woods, M., and AJ, S. (2018). Australian geological provinces 2018.01 edition. *Geoscience Australia, Canberra*.

Reid, A. (2019). The olympic cu-au province, gawler craton: a review of the lithospheric architecture, geodynamic setting, alteration systems, cover successions and prospectivity. *Minerals*, 9(6):371.

Sheehan, A. F., Abers, G. A., Jones, C. H., and Lerner-Lam, A. L. (1995). Crustal thickness variations across the colorado rocky mountains from teleseismic receiver functions. *Journal of Geophysical Research: Solid Earth*, 100(B10):20391–20404.

Shepard, D. (1968). A two-dimensional interpolation function for irregularly-spaced data. In *Proceedings of the 1968 23rd ACM national conference*, pages 517–524.

Southgate, P., Neumann, N., and Gibson, G. (2013). Depositional systems in the mt isa inlier from 1800 ma to 1640 ma: Implications for zn–pb–ag mineralisation. *Australian Journal of Earth Sciences*, 60(2):157–173.

Srinivas, D., Srinagesh, D., Chadha, R., and Ravi Kumar, M. (2013). Sedimentary thickness variations in the indo-gangetic foredeep from inversion of receiver functions. *Bulletin of the Seismological Society of America*, 103(4):2257–2265.

Tao, K., Liu, T., Ning, J., and Niu, F. (2014). Estimating sedimentary and crustal structure using wavefield continuation: theory, techniques and applications. *Geophysical Journal International*, 197(1):443–457.

Tauzin, B., van der Hilst, R. D., Wittlinger, G., and Ricard, Y. (2013). Multiple transition zone seismic discontinuities and low velocity layers below western united states. *Journal of Geophysical Research: Solid Earth*, 118(5):2307–2322.

Vinnik, L. (1977). Detection of waves converted from p to sv in the mantle. *Physics of the Earth and planetary interiors*, 15(1):39–45.

Wade, B., Kelsey, D., Hand, M., and Barovich, K. (2008). The musgrave province: stitching north, west and south australia. *Precambrian Research*, 166(1-4):370–386.

Wakelin-King, G. and White, S. (2016). The national heritage potential of landscapes within the australian drylands. *Geoheritage*, 8(2):105–118.

Wang, M., Hubbard, J., Plesch, A., Shaw, J. H., and Wang, L. (2016). Three-dimensional seismic velocity structure in the sichuan basin, china. *Journal of Geophysical Research: Solid Earth*, 121(2):1007–1022.

Wessel, P., Luis, J., Uieda, L., Scharroo, R., Wobbe, F., Smith, W., and Tian, D. (2019). The generic mapping tools version 6. *Geochemistry, Geophysics, Geosystems*, 20(11):5556–5564.

Wopfner, H. et al. (1969). *Depositional history and tectonics of South Australian sedimentary basins*. Economic Commission for Asia and the Far East Committee on Industry and ....

Yeates, A., Gibson, D., Towner, R., and Crowe, R. (1984). Regional geology of the onshore canning basin, wa.

Yeck, W. L., Sheehan, A. F., and Schulte-Pelkum, V. (2013). Sequential h-κ stacking to obtain accurate crustal thicknesses beneath sedimentary basins. *Bulletin of the Seismological Society of America*, 103(3):2142–2150.

Yu, Y., Song, J., Liu, K. H., and Gao, S. S. (2015). Determining crustal structure beneath seismic stations overlying a low-velocity sedimentary layer using receiver functions. *Journal of Geophysical Research: Solid Earth*, 120(5):3208–3218.

Zang, W.-L., Jago, J., Alexander, E., and Paraschivoiu, E. (2004). A review of basin evolution, sequence analysis and petroleum potential of the frontier arrowie basin, south australia.

Zelt, B. and Ellis, R. (1999). Receiver-function studies in the trans-hudson orogen, saskatchewan. *Canadian Journal of Earth Sciences*, 36(4):585–603.

Zheng, T., Zhao, L., and Chen, L. (2005). A detailed receiver function image of the sedimentary structure in the bohai bay basin. *Physics of the Earth and Planetary Interiors*, 152(3):129–143.

Author postal address

Shubham Agrawal

142 Mills Road, ANU, Acton, ACT 0200, Australia.

Caroline Eakin

142 Mills Road, ANU, Acton, ACT 0200, Australia.

John O’Donnell

Level 4, 11 Waymouth Street, Adelaide, South Australia 5000, Australia.

List of Figures

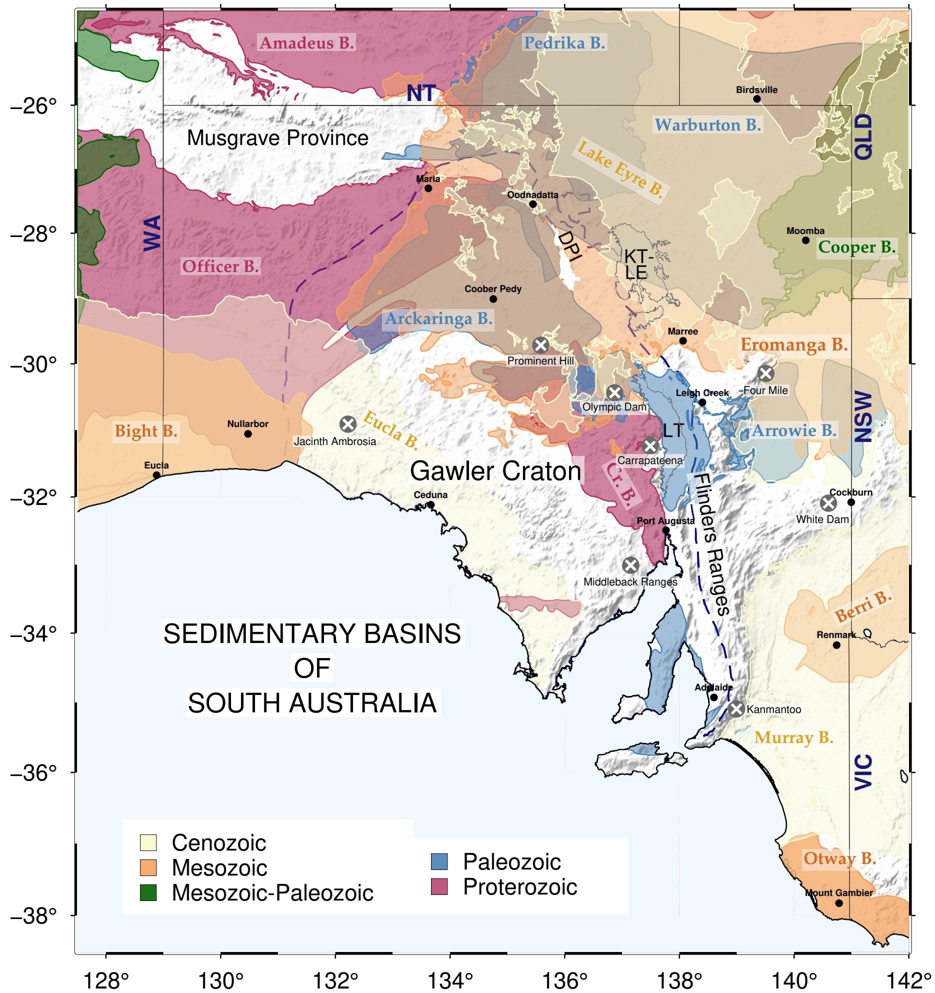

Figure 1. A comprehensive on-shore sedimentary basin map of South Australia. Basin information is acquired from the Geoscience Australia database (Raymond et al., 2018). Gray circles with white crosses are major approved/operating mines (see Data and Resources Section). The dashed blue line is the inferred boundary of the Gawler Craton. Abbreviations are as follows - Cr.B: Cariewerloo Basin, DPI: Denison and Peake inliers, KT-LE: Kati Thanda-Lake Eyre, LT: Lake Torrens, WA: Western Australia, NT: Northern Territory, QLD: Queensland, NSW: New South Wales, VIC: Victoria. For the color version of this figure, refer to the electronic edition.

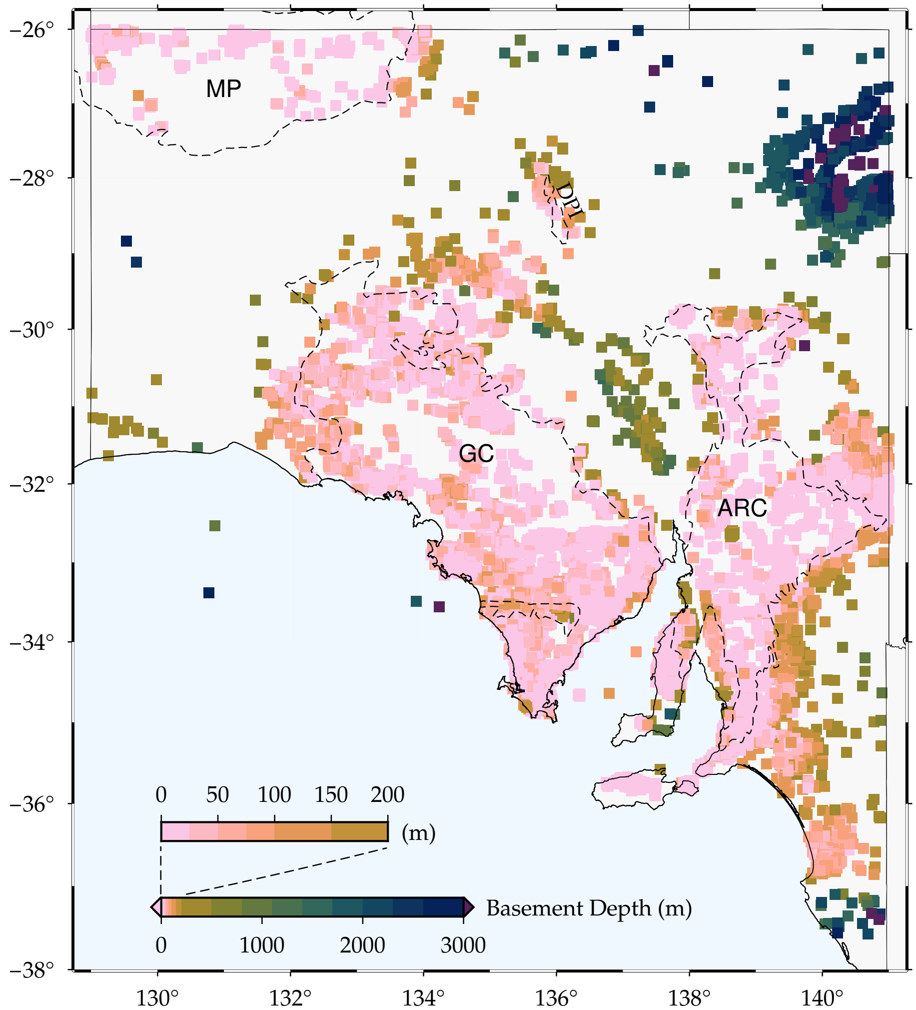

Figure 2. Individual borehole basement depth measurements (colored squares) for the state of South Australia (see Data and Resources Section). The black dashed lines are geological provinces (MP: Musgrave Province; GC: Gawler Craton; ARC: Adelaide Rift Complex) with little or no sediment cover (Raymond et al., 2018). The color scale is adjusted in the upper 200 km to encapsulate the variations in depth. For the color version of this figure, refer to the electronic edition.

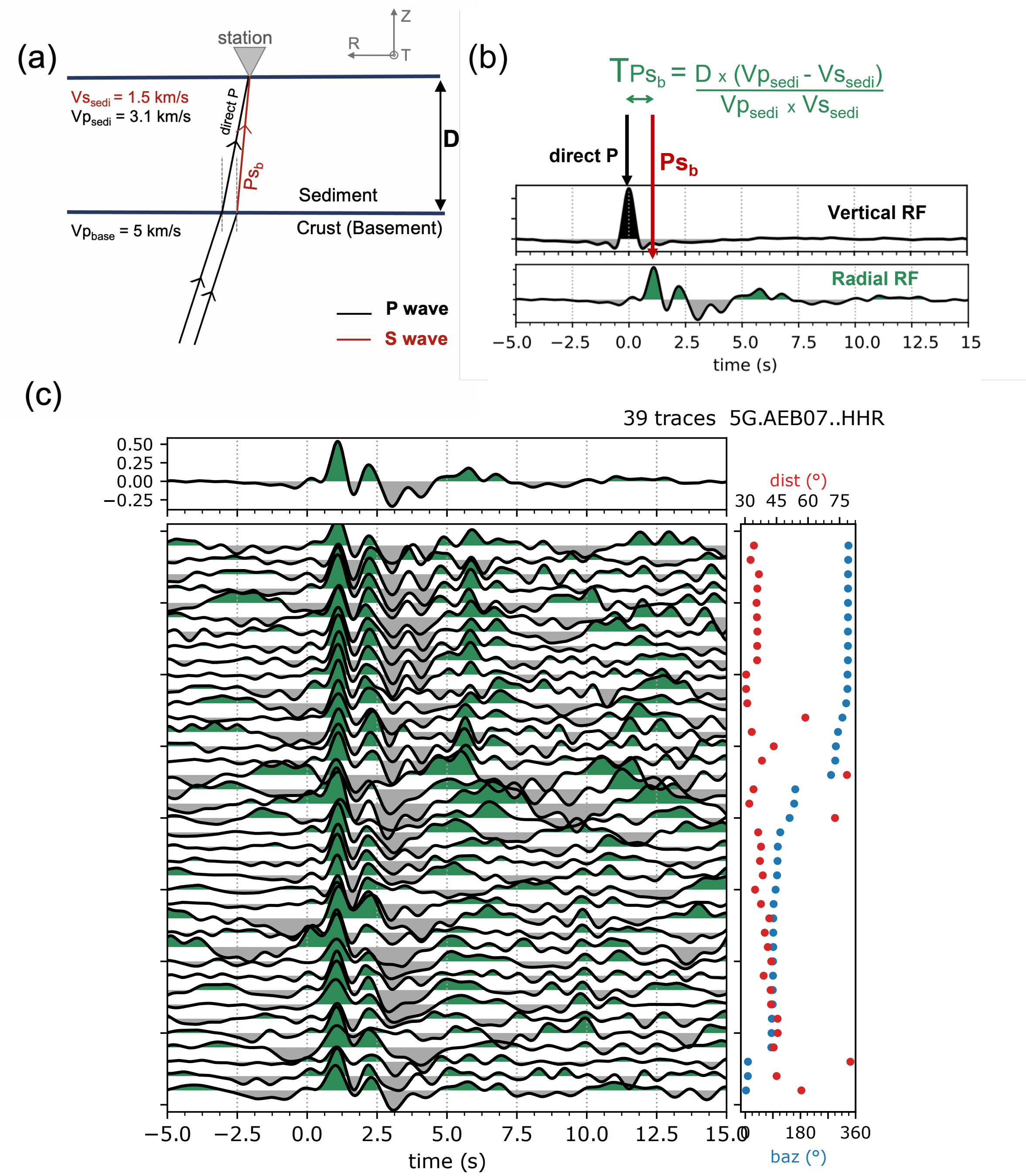

Figure 3. a) Schematic ray paths of P and S waves traversing a sediment layer (of thickness D) in response to an incoming P wave from an epicentral distance of 60° for the shown velocity structure. b) An example of $T_{\mathrm{Ps_b}}$ estimation from receiver functions at typical station AEB07. The station is located on thick sediment cover (see Figure 4 for location), hence the significant delay in the $\mathrm{Ps_b}$ phase relative to direct P. The formula for $T_{\mathrm{Ps_b}}$ is derived assuming vertical incidence of P and S waves beneath the station. c) Individual receiver functions that passed the quality control for station AEB07, which were used to calculate the stacked receiver function. The right panel provides epicentral distance (red dots) and backazimuth (blue dots) values for each receiver function. For the color version of this figure, refer to the electronic edition.

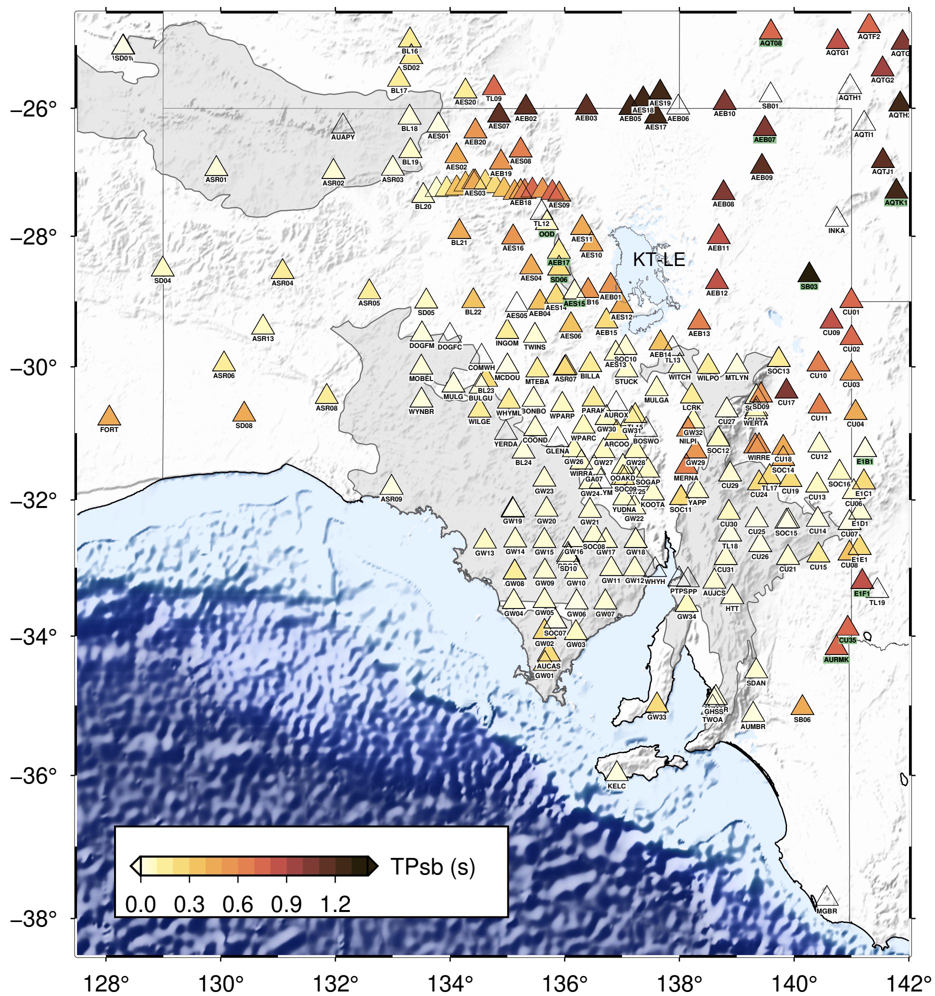

Figure 4. Values for times of arrivals of P-to-S converted phase ($T_{\mathrm{Ps_b}}$) at the basement for seismic stations in South Australia. $T_{\mathrm{Ps_b}}$ values are estimated from receiver functions, as illustrated in Figure 3. Transparent triangles are stations where receiver functions did not pass quality control. Stations names highlighted with green are stations discussed in the text. Gray shaded areas are the same as the dashed geological provinces in Figure 2. KT-LE: Kati Thanda-Lake Eyre. For the color version of this figure, refer to the electronic edition.

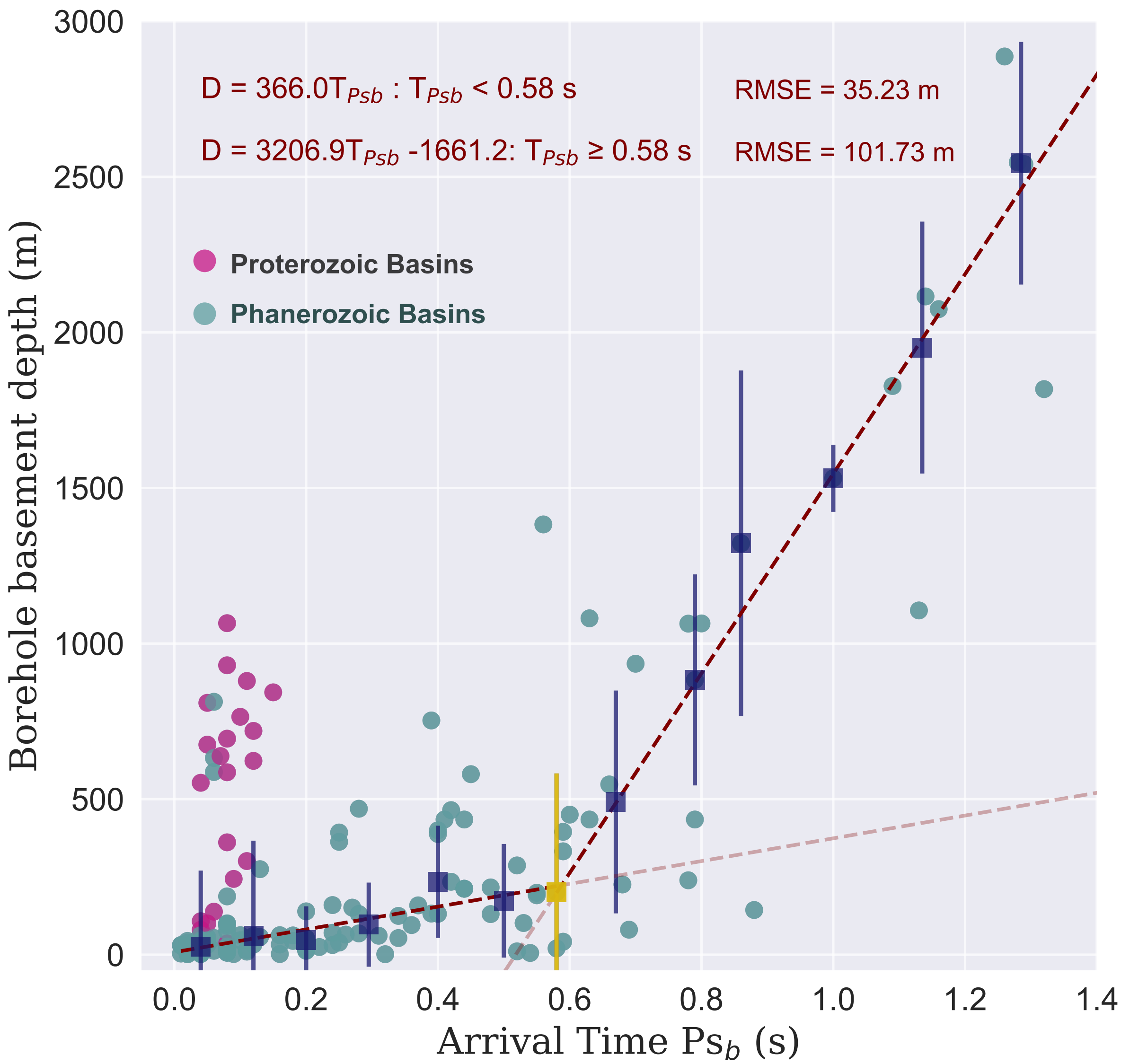

Figure 5. Statistical comparison of the receiver function estimated $T_{\mathrm{Ps_b}}$ and borehole basement depth beneath 182 seismic stations, plotted as circles. Turquoise circles are stations situated atop Phanerozoic Basins while pink on Proterozoic Basins. Dark blue squares are the binned median values for every 0.9 s, with vertical solid blue lines representing the standard deviation. The yellow square denotes the point of inflection in the data, about which two linear equations (maroon dotted lines with equations at top) are regressed. RMSE: Root Mean Square Error. For the color version of this figure, refer to the electronic edition.

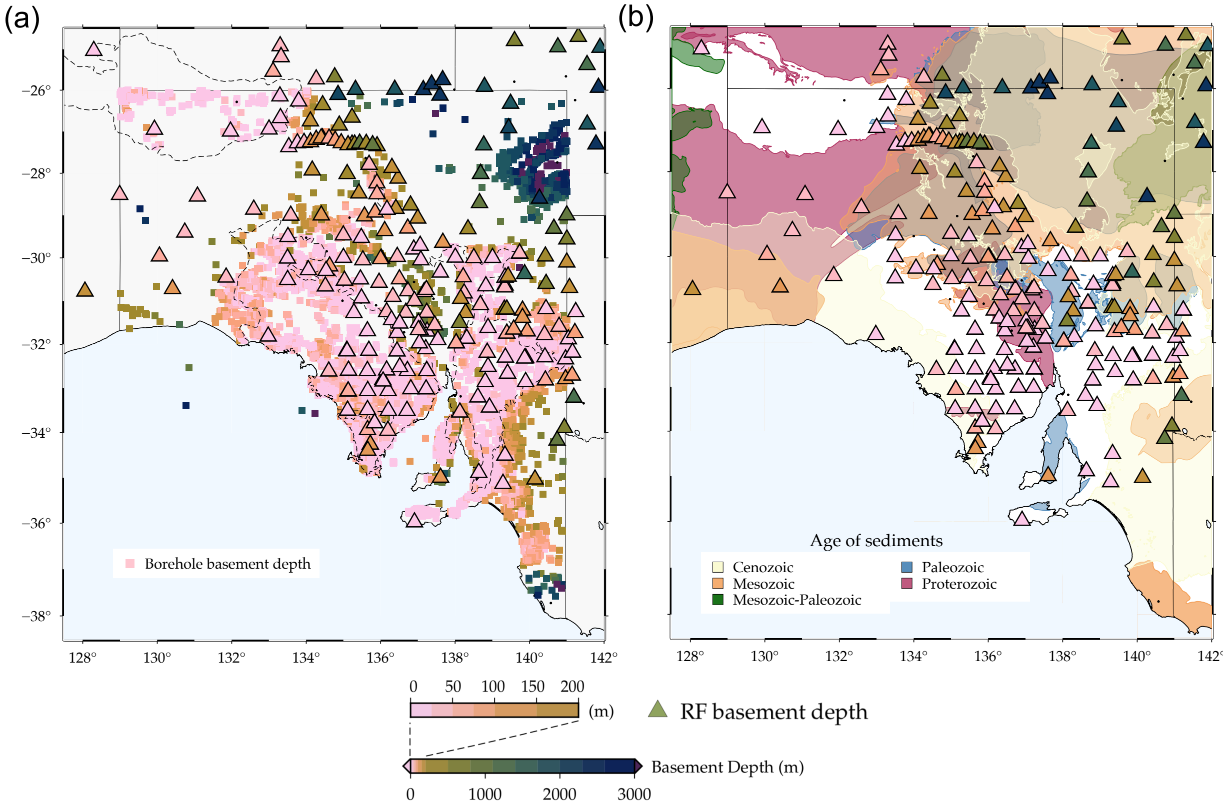

Figure 6. Receiver function estimated basement depth (colored triangles) juxtaposed with (a) borehole measurements (same as Figure 2) and (b) sedimentary basins (same as Figure 1). The black dots are stations that didn't pass quality control. It is to be noted that in (b), the basins are colored by the age of sediments, while the stations are colored according to the RF basement depth, given by the legend below the figure. For the color version of this figure, refer to the electronic edition.